Valley-contrasting transport of the coupling between spin and orbital angular momentum in ferromagnetic transition metal dichalcogenides

Shilei Ji,[1,*] Weiyi Pan,[2] Chuye Quan,[1] Xiaoyang He,[1] Chen Chen,[1] Jianping Yang,[1] and Xing'ao Li[1,3,†]

[1]*School of Science, Jiangsu Provincial Engineering Research Center of Low Dimensional Physics and New Energy, Nanjing University of Posts and Telecommunications (NJUPT), Nanjing 210023, China*

[2]*State Key Laboratory of Low Dimensional Quantum Physics and Department of Physics, Tsinghua University, Beijing 100084, China*

[3]*School of Physics and Electronic Information, Jiangsu Second Normal University, Nanjing 210013, China*

(Received 8 May 2024; revised 9 July 2024; accepted 22 July 2024; published 14 August 2024)

Transition metal dichalcogenides exhibit intrinsic spin-orbit coupling that opens spin splittings in valleys, resulting in spin and orbital polarized bands. Energy valleys driven by electric fields can generate spin (anomalous) Hall effect and orbital Hall effect. Here we focus on ferromagnetic materials and demonstrate that the transport of spin and orbital Hall effects can be attributed to the spin-orbit coupling, which can be characterized by spin-orbital polarization. Driven by an electric field, orbital and spin angular momentum appear at both ends of the sample through corresponding Hall effect, leading to the formation of valley-contrasting spin-orbital polarization states. Based on the spin and orbital transport analysis, we propose the intrinsic magnetic moment as a method to manipulate the spin-orbital polarization states, which enables the four-state switching of the angular momentum at the edge of sample. Moreover, due to the conservation of angular momentum, circularly polarized optical pumping can be used instead of an electric field to selectively excite the orbital and spin angular momentum. Subsequently, we argue that the sign-reversal spin-orbital polarization requires not only spin-orbit coupling effect but also the simultaneous broken time-reversal and inversion symmetries.

DOI: 10.1103/PhysRevB.110.075418

I. INTRODUCTION

Orbital angular momentum serves as a crucial information carrier in the generation and transportation processes within the orbital Hall effect (OHE) [1–6]. This phenomenon is facilitated by the intricate orbital structure of crystals, where an in-plane electric field induces orbital Berry curvature, consequently eliciting pure orbital polarized currents perpendicular to the electric field [3,7–11]. The manipulation and transmission of information through the orbital degrees of freedom represent a pivotal frontier in the realm of orbitronics devices [4,12–15]. OHE presents an advantageous investigative avenue as it operates independently of spin-orbit coupling (SOC) effects, rendering weakly SOC single atoms and compounds as prime candidates for discerning and characterizing this phenomenon [3,7,11,16].

Transition metal dichalcogenides (TMDs) are considered ideal two-dimensional systems for studying OHE due to the valley orbital magnetic moments induced by inversion symmetry breaking [8,17–21]. TMDs like MoS_2 break inversion symmetry at the sublattice level, resulting in two nonequivalent valleys, leading to an intrinsic OHE [22–25]. Simultaneously, the OHE in the insulating gap possesses a nonzero orbital Chern number [9,18,19]. Similarly to the quantum spin Hall effect, the valley orbital magnetic moment generates corresponding angular momentum with opposite trajectory motion, which is dependent on the sign of orbital Chern number [16,26]. The SOC effect in TMDs can open up spin splitting in the two valleys, resulting in the spin Hall effect (protected by time-reversal symmetry) and the anomalous Hall effect (time-reversal symmetry breaking) [26–28]. Earlier studies have demonstrated that the Hall current generated through the anomalous Hall effect (AHE) carries spin angular momentum [29–33]. On the other hand, current driven by orbital Hall effect can carry orbital angular momentum, which is connected to the orbital texture in the valleys [3,4,34,35].

The angular momentum, driven by SHE and OHE, generates spin and orbital torques at the edges of sample, manipulating the spin polarization of the proximity ferromagnetic layer through the SOC effect [4,36]. Due to the opposite signs of spin or anomalous Hall conductivity in two valleys, the OHE in TMDs is much stronger than the spin Hall effect (SHE) and AHE [9]. However, the Berry curvature for each valley are comparable to the orbital Berry curvature, indicating that the spin and orbital currents excited at each valley are equivalent [18,37]. According to the SOC effect [3,4,38], the Hamiltonian H_{so} couples the spin angular momentum $\hat{S}$ with orbital angular momentum $\hat{L}$,

$$H_{so} = \frac{\lambda_{so}}{\hbar^2}\hat{L}\cdot\hat{S}, \tag{1}$$

where λ_{so} is the strength of SOC effect. Due to the presence of SOC effects in transition metals, synergistic effects of orbitals and spins are important and may have novel observable physical effects. Further study is still needed to explore the valley

*Contact author: njuptjishilei@outlook.com
†Contact author: lxahbmy@126.com

transport of spin and orbital angular momentum influenced by the SOC effect.

Here we use $k \cdot p$ model and density functional theory (DFT) to study the angular momentum accumulation of OHE and SHE. We uncover that each valley in ferromagnetic orbital Hall insulators exhibits spin and orbital angular momentum, which can couple into $\langle \hat{L}_z \cdot \hat{S}_z \rangle$ through the SOC effect. Linear response calculations indicate that the OHE and SHE in ferromagnetic orbital Hall insulators carry corresponding angular momentum during transport and scatter perpendicular to the direction of the electric field through Berry curvature. Numerical and analytical calculations indicate that there are sign-reversal $\langle \hat{L}_z \cdot \hat{S}_z \rangle$ at the left and right sides, which is related to valley index and spin polarization. Based on valley-contrasting circular dichroism, we propose using circularly polarized light to select the sign of $\langle \hat{L}_z \cdot \hat{S}_z \rangle$ and put forward a method for four-state information processing. Finally, we demonstrate that the occurrence of sign-reversal $\langle \hat{L}_z \cdot \hat{S}_z \rangle$ requires satisfying: (i) a non-negligible SOC effect and (ii) the broken time-reversal and inversion symmetries.

II. $k \cdot p$ MODEL ANALYSIS

Starting from the ferromagnetic (FM) TMD monolayers, we construct a general two-band $k \cdot p$ model for trigonal prismatic lattices [23]. The detailed Hamiltonian at the basis of $\psi_v^\tau = (|d_{x^2-y^2}\rangle + i\tau|d_{xy}\rangle)/\sqrt{2}$ and $\psi_c^\tau = |d_{z^2}\rangle$ can be written as:

$$H_{\text{eff}} = t(\tau\hat{\sigma}_x k_x + \hat{\sigma}_y k_y) + \frac{\Delta}{2}\hat{\sigma}_z - \tau\hat{s}_z\lambda_v\frac{\hat{\sigma}_z - 1}{2}. \quad (2)$$

Here Δ is the band gap of the valley, $\tau = \pm 1$ is the valley index for K_+ and K_- valleys, and t is the nearest-neighbor intralayer hopping. Moreover, $2\lambda_v$ is the band splitting introduced by SOC effect at the valance band maximum, and $s_z = \pm 1$ represents the spin index for z axis. $\hat{\sigma}_i$ $(i = x, y, z)$ is Pauli matrices. The eigenvalues at two valleys are expressed as: $E_\pm = (E_0 \pm \sqrt{4t^2k^2 + \Delta_{\tau,s_z}^2})/2$. Here we use $E_0 = \tau s_z \lambda_v$, $k^2 = k_x^2 + k_y^2$, and $\Delta_{\tau,s_z} = \Delta - \tau s_z \lambda_v$, respectively. The SOC effect breaks spin degeneracy, which leads to the emergence of spin-polarized valleys [39]. Also, according to the basis function $\psi_v^\tau = (|d_{x^2-y^2}\rangle + i\tau|d_{xy}\rangle)/\sqrt{2}$ on the valence band, the valleys are orbital polarization. Here we calculate the expectation values of spin and orbital angular momentum on the two valleys [36],

$$\langle \hat{X}_z \rangle = \langle \psi_{n\boldsymbol{k}} | \hat{X}_z | \psi_{n\boldsymbol{k}} \rangle, \quad (3)$$

where $\hat{X}_z = \hat{S}_z$ and $\hat{X}_z = \hat{L}_z$ are spin and orbital angular momentum. The orbital angular momentum near the valance valley is approximately $\pm 2\hbar$. The spin angular momentum on the valley under two spin-polarization ($s_z = \pm 1$) is denoted as $\langle \hat{S}_z \rangle = \pm\hbar/2$. We observe that under two different spin cases, the orbital angular momentum remains unchanged, while the spin angular momentum is opposite.

The valleys with spin and orbital polarization can excite carriers with spin and orbital angular momentum. Here, inspired by the Hamiltonian of H_{so}, we can adopt a new notation, namely $\langle \hat{L}_z \cdot \hat{S}_z \rangle$, to represent this carrier state [3,4,36,38]. Using $\hat{X}_z = \hat{L}_z \cdot \hat{S}_z$ in Eq. (3), we can obtain the spin-orbital expectation values for two spin cases. We can find that, the spin-orbital expectation values of holes can be written as $\langle \hat{L}_z \cdot \hat{S}_z \rangle_\tau^{s_z} = \tau s_z \hbar^2$. For the same spin angular momentum (such as broken time-reversal symmetry), the spin-orbital polarization is opposite at two valleys.

In ferrovalley materials, when an electric current is applied in the longitudinal direction, the spin(orbital)-polarized electrons will be deflected laterally, and the direction of deflection is related to the valley index. This results in the accumulation of spin(orbital)-polarized electrons perpendicular to the applied electric field, which is known as the SHE(OHE). Due to the SOC effect, the $\langle \hat{L}_z \cdot \hat{S}_z \rangle_\tau^{s_z}$ located at two valleys will be excited by SHE and OHE with the Berry curvature [40]

$$\Omega_n^{\hat{J}_y}(\boldsymbol{k}) = -2\hbar \sum_{n \neq n'} \frac{\text{Im}\langle \psi_{n\boldsymbol{k}} | \hat{v}_x | \psi_{n'\boldsymbol{k}} \rangle \langle \psi_{n'\boldsymbol{k}} | \hat{J}_y | \psi_{n\boldsymbol{k}} \rangle}{(E_{n'} - E_n)^2}, \quad (4)$$

where $\hat{v}_i$ $(i = x, y)$ is the velocity operator along the k_i direction, with $\hat{v}_i = \frac{1}{\hbar}\frac{\partial H}{\partial k_i}$. The angular momentum operator $\hat{J}_y$ is defined as $\hat{J}_y = (\hat{v}_y\hat{X}_z + \hat{X}_z\hat{v}_y)/2$, where $\hat{X}_z$ is $\hat{L}_z = \text{diag}(2\hbar\tau, 0)$ for the orbital angular momentum operator and $\hat{S}_z = \text{diag}(s_z\hbar/2, s_z\hbar/2)$ for spin angular momentum operator. In addition, $\hat{v}_y$ can be substituted for $\hat{J}_y$ in AHE calculations [41]. The corresponding spin Berry curvature $\Omega_n^{S,\tau}$ and orbital Berry curvature $\Omega_n^{O,\tau}$ can be simplified as

$$\Omega_n^{S,\tau}(\boldsymbol{k}) = \frac{\tau s_z t^2 \Delta_{\tau,s_z}}{\left(4t^2k^2 + \Delta_{\tau,s_z}^2\right)^{3/2}} = \frac{1}{2}\tau s_z \Omega_n^{O,\tau}(\boldsymbol{k}). \quad (5)$$

The sign of orbital Berry curvature is independent of the spin and valley index, which demonstrate that the transport of orbital angular momentum cannot be manipulated through spin and valley polarization. Meanwhile, the sign of spin Berry curvature is not only related to spin but also associated with valleys. The spin Berry curvature in ferromagnetic TMDs has opposite signs at two valleys. The Berry curvature is equivalent to a magnetic field in momentum space, and the direction of anomalous velocity is determined by the sign of corresponding angular momentum, Berry curvature, and electric field. As shown in Figs. 1(a) and 1(b), both OHE and SHE exhibit valley-dependent transport characteristics. However, they generate different types of currents. Valley-contrasting orbital angular momentum accumulates on the left and right sides to form pure orbital currents, whereas the same spin angular momentum, driven by valley-contrasting spin Berry curvature, forms spin-polarized currents.

Under the SOC effect, the spin and orbital angular momentum on both sides of the ferromagnetic material in Fig. 1(c) couple to $\langle \hat{L}_z \cdot \hat{S}_z \rangle$ [6,36], whose sign is the same as the expectation value of spin-orbital in their valleys. Switching the spin polarization can generate opposite spin angular momentum. In the spin-down configuration as shown in Fig. 1(d), there is a switch in the sign of $\langle \hat{L}_z \cdot \hat{S}_z \rangle$ compared to that in spin-up configuration. Therefore, ferromagnetic TMDs under electric field drive have four spin-orbital states with $\langle \hat{L}_z \cdot \hat{S}_z \rangle_\tau^{s_z} = \tau s_z \hbar^2$, switching between these four states through spin and energy valleys. The different states in the two valleys can be detected through electrical or optical methods [24,42,43].

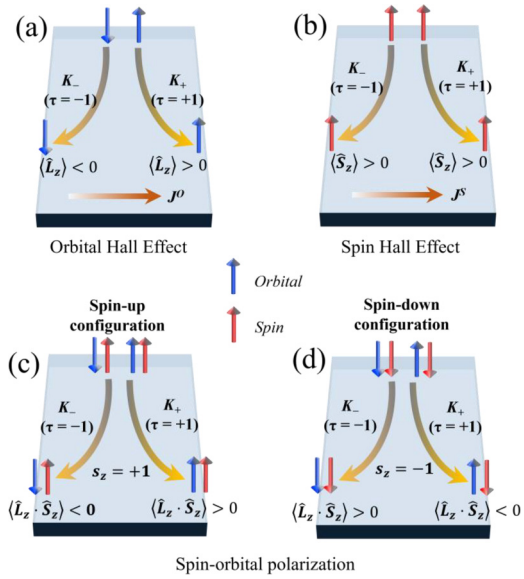

FIG. 1. The diagram of (a) orbital Hall effect, (b) spin Hall effect, and [(c) and (d)] spin-orbital polarization in ferromagnetic TMDs. The magnetic moment in (a)–(c) is spin-up configuration, while panel (d) represents spin-down configuration. Blue and red arrows represent orbital angular moment $\langle \hat{L}_z \rangle$ and spin angular momentum $\langle \hat{S}_z \rangle$, respectively. J^α is the Hall current, where α is orbital (O) and spin (S).

III. DFT SIMULATIONS

A. Spin-orbital polarization on valleys

Building on the conclusions mentioned above, we select a suitable TMD to implement our idea, 2H-VS_2, which has been demonstrated to exhibit intrinsic ferromagnetism and valley polarization [44–46]. The atomic structure is plotted in Fig. S1 [47], the sublattices of V and S atoms, breaking the inversion symmetry, form a trigonal lattice structure with the D_{3h} space group symmetry. The D_{3h} crystal field of V atom splits the $3d$ orbitals into nondegenerate A' orbital (d_{z^2}) and twofold degenerate E' orbitals (d_{xy} and $d_{x^2-y^2}$) at lower energy, as well as higher-energy E'' orbitals (d_{xz} and d_{yz}). An unpaired electron occupy the lower-energy A' orbital, giving rise to an intrinsic magnetic moment of $1\mu_B$, breaking time-reversal symmetry.

To demonstrate the spin and orbital angular momentum ($\hat{S}_z$ and $\hat{L}_z$), we construct the Wannier function based on first-principles calculations in Figs. 2(a) and 2(b) to simulate the expectations value of Eq. (3), respectively [48–51]. The orbital angular momentum near two valleys mainly comes from the E' orbital in the valence band, while the sign relies on the valley index. The spin angular momentum distribution, on the other hand, is independent of the valleys. The spin-down channels are suppressed due to the appearance of intrinsic magnetic moment in VS_2. Therefore the spin angular momentum near the Fermi energy consists of $\langle \hat{S}_z \rangle = \hbar/2$. As discussed above, we can use $\langle \hat{L}_z \cdot \hat{S}_z \rangle$ to demonstrate the coupling between spin and orbital angular momentum. The detailed $\langle \hat{L}_z \cdot \hat{S}_z \rangle$ is plotted in Fig. 2(c). The sign of $\langle \hat{L}_z \cdot \hat{S}_z \rangle$ depends on the valley index, and its numerical value from first-principles calculations is consistent with the result of analytical calculations in Sec. II. Since the orbital angular momentum is only related to the valley, spin-orbital polarization of opposite sign appear when the magnetic moment switches to Fig. 2(d).

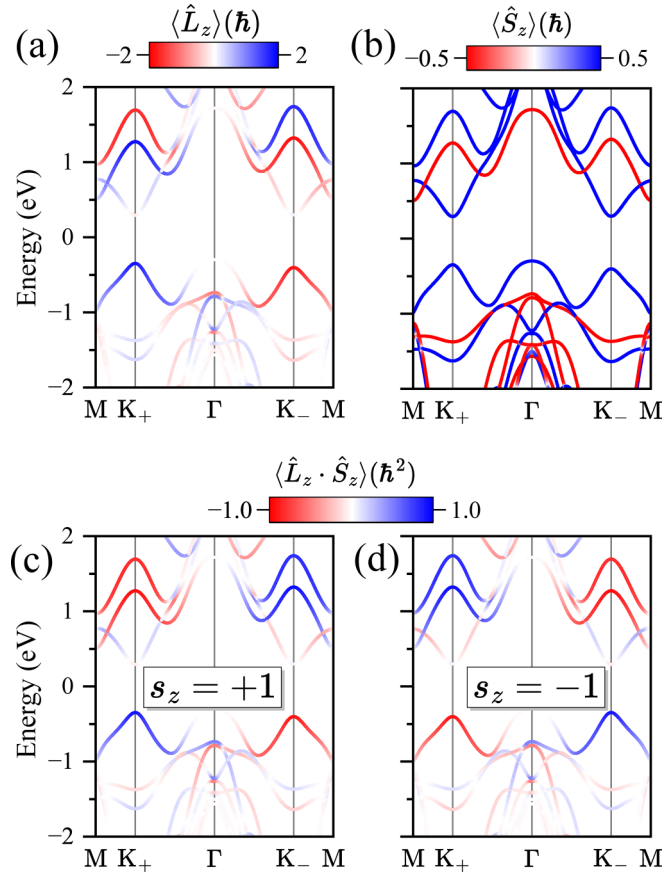

FIG. 2. (a) The orbital, (b) spin, and [(c) and (d)] spin-orbital structure of VS_2, where (c) and (d) represent spin-up and spin-down configuration, respectively.

B. Transport of spin and orbital angular momentum

Due to the broken inversion and time-reversal symmetries, the two valleys have nonzero orbital and spin Berry curvature, which is equivalent to a magnetic field in momentum space. By applying an in-plane electrical field E, the corresponding Berry curvature can generate a Lorentz force perpendicular to the direction of electric field, leading to carrier exhibiting an anomalous velocity [52,53]. In Figs. 3(a) and 3(b), first-principles calculations show that there are extreme values of orbital and spin Berry curvatures on both valleys, which results from the magnetic quantum number $m_l = \pm 2$ for both valleys. In addition, it is found that the numerical values of spin and orbital Berry curvature are comparable, indicating the presence of OHE and SHE in VS_2 that cannot be ignored.

For a two-dimensional system, the orbital Hall conductivity (OHC) σ_{xy}^O and spin Hall conductivity (SHC) σ_{xy}^S can be calculated by

$$\sigma_{xy}^{\alpha} = \frac{e}{\hbar} \sum_n \int_{\mathrm{BZ}} \frac{d^2k}{(2\pi)^2} f_{nk} \Omega_n^{\alpha}(\boldsymbol{k}), \tag{6}$$

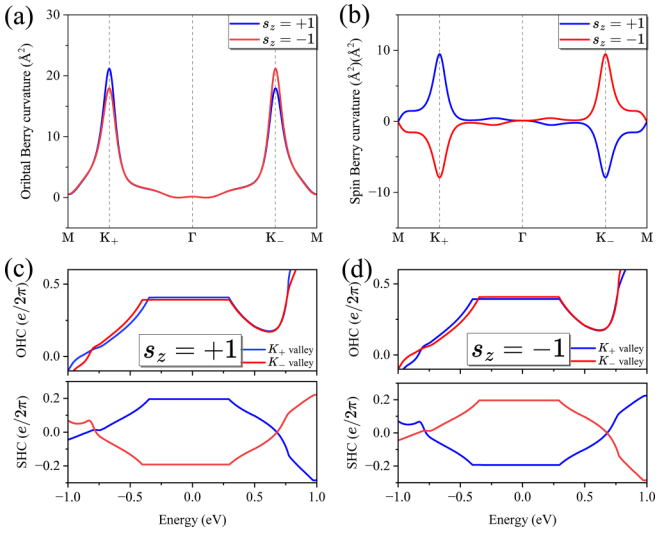

FIG. 3. (a) The orbital Berry curvature, and (b) spin Berry curvature of VS_2 with the spin-up (blue) and spin-down (red) configurations. [(c) and (d)] The orbital and spin Hall conductivity of two spin configurations. Blue and red lines in (c) and (d) represent the K_+ and K_- valleys, respectively.

where the superscript α is orbital (O) and spin (S). Moreover, BZ represents the Brillouin zone and f_{nk} is the Fermi-Dirac distribution.

The p-d orbital hybridization on the valley is weak due to the limited contribution of the S-p orbitals in Fig. S1 [47]. The OHE mainly originates from the valley orbital magnetic moment in the noncentrosymmetric systems. The relation between the valley orbital magnetic moment $\mathbf{M}(\boldsymbol{k})$ and symmetry can be written as [54,55]:

$$\mathbf{M}(\boldsymbol{k}) = \mathbf{M}(-\boldsymbol{k}) \text{ (Inversion symmetry present)}$$
$$\mathbf{M}(\boldsymbol{k}) = -\mathbf{M}(-\boldsymbol{k}) \text{ (Time-reversal symmetry present).} \quad (7)$$

The existence of valley orbital magnetic moment requires the breaking of either symmetries. The sublattices of V and S atoms in VS_2 give rise to a broken inversion symmetry, resulting in the valley-contrasting orbital structure in Fig. 2(a). Meanwhile, the SOC effect, arising from ferromagnetic transition metal atoms, results in the spin magnetic moments and SHE.

In Fig. 3(c), we conduct numerical calculations of OHE and SHE based on the electronic structure using first-principles methods combined with Eq. (4). It can be seen that in the insulating bandgap of VS_2, the OHC on both valleys is 0.5 $e/2\pi$. According to the Chern number $C_\alpha = \frac{1}{2\pi}\int_{BZ} d^2\boldsymbol{k}\Omega_n^\alpha(\boldsymbol{k})$, we can find that the orbital Chern number C_L on both valleys is 1/2, indicating that VS_2 is an orbital Hall insulator. At the same time, the spin down of the valleys is suppressed due to the intrinsic ferromagnetism of VS_2 with the spin Chern number of $C_S = \pm 1/4$. The signs of OHC and SHC represent the directions of orbital polarization current and spin polarization current, respectively, which can be defined as J^α based on Fig. 1. For the spin-up configuration in Fig. 3(c), the opposite orbital angular momentum at two valleys results in the $\langle \hat{L}_z \rangle > 0$ ($\langle \hat{L}_z \rangle < 0$) accumulating on the right (left) side of VS_2. Meanwhile, $\langle \hat{S}_z \rangle > 0$ accumulates on both two sides due to opposite SHC at two valleys. The spin-orbital polarization can be written as $\langle \hat{L}_z \cdot \hat{S}_z \rangle > 0$ on the right side and $\langle \hat{L}_z \cdot \hat{S}_z \rangle < 0$ on the left side.

In ferromagnetic TMDs, the orbital angular momentum, related to the magnetic quantum number and valley index, is protected from external field by the trigonal crystal field. Therefore, it is more challenging to manipulate orbital angular momentum by external field than spin angular momentum. Techniques such as gate voltage and magnetic fields can be employed to alter the direction of magnetic moments, thereby changing the distribution of spin angular momentum. As depicted in Fig. 3(d), there is a switch in the sign of SHC on two valleys. Therefore, the right side has $\langle \hat{L}_z \cdot \hat{S}_z \rangle < 0$, in contrast to the left side. Based on Figs. 2(c) and 2(d) and Figs. 3(c) and 3(d), we find that the spin-orbital polarization on the left and right sides of the sample is related to the electronic structure.

The spin polarization can flexibly switch the sign of $\langle \hat{L}_z \cdot \hat{S}_z \rangle$, thereby forming four states. According to Ref. [4,36], the injection of orbital and spin angular momentum can respectively create orbital and spin torques. Due to its ability to generate four types of spin-orbital polarization, TMDs can serve as an ideal platform for investigating the spin and orbital torques through spin polarization and valley selection. Furthermore, the accumulation of angular momentum in the excited state of TMDs is consistent with the spin-orbital polarization weight of the ground state electronic structure.

IV. CIRCULARLY POLARIZED OPTICAL PUMPING

Interband direct transitions of optically excited electron-hole pairs adhere to the principles of angular momentum conservation. In a hexagonal lattice, the contributions of opposite orbital angular momentum on the band determine distinct optical selection rules, namely, opposite circular dichroism. This can be is characterized by the circular polarization degree of the optical interband absorption between the valence and conduction bands $\eta(\boldsymbol{k})$,

$$\eta(\boldsymbol{k}) = \frac{|P_+(\boldsymbol{k})|^2 - |P_-(\boldsymbol{k})|^2}{|P_+(\boldsymbol{k})|^2 + |P_-(\boldsymbol{k})|^2}, \quad (8)$$

where $P_\pm(\boldsymbol{k})$ is the coupling strength with $\sigma_\pm$ optical fields and $\sigma_\pm$ is the left- and right-circular polarized lights. The detailed the coupling strength $P_\pm(\boldsymbol{k})$ can be given by $P_\pm(\boldsymbol{k}) = P_x(\boldsymbol{k}) \pm iP_y(\boldsymbol{k})$, where $P_\alpha(\boldsymbol{k}) = m_0\langle\psi_{ck}|\frac{1}{\hbar}\frac{\partial H}{\partial k_\alpha}|\psi_{vk}\rangle$. First, we analyze the circular polarized optical absorption from our $k \cdot p$ model. The orbital contributions of the conduction and valance bands are A' and E', respectively. For the transition around two valleys, the coupling strength for our $k \cdot p$ model can be written as

$$|P_\pm(\boldsymbol{k})|^2 = \frac{m_0^2 t^2}{\hbar^2}\left[1 \pm \tau \frac{\Delta_{\tau,s_z}}{\left(4t^2k^2 + \Delta_{\tau,s_z}^2\right)^{1/2}}\right]^2. \quad (9)$$

Due to $\Delta_{\tau,s_z} \gg t \cdot k$, we can obtain that, close to the center of K_+/K_- valley, the interband transition is coupled with σ_+/σ_- polarized light, respectively. Then we use the kubo method to calculate the optical absorption between the valance and conduction bands at the two valleys in Fig. 4. There are two peaks at optical absorption, which are consistent with the band gaps at two valleys. The carriers at K_+

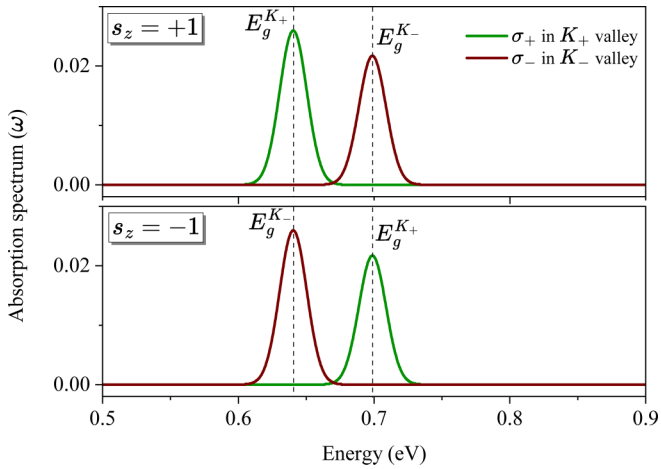

FIG. 4. The circular polarized light absorption for spin-up and spin-down configurations

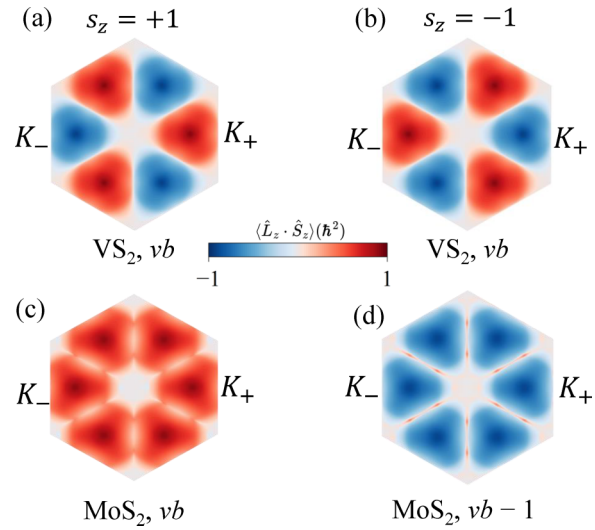

FIG. 5. The spin-orbital polarization of [(a) and (b)] VS_2 and [(c) and (d)] MoS_2. [(c) and (d)] The highest valence band and the second-highest valence band (vb).

valley can be excited by left-circular polarized light, while that at K_- valley can be excited by right-circular polarized light. Moreover, the optical selection rule is independent of the spin-polarization. When flipping the spin of 2H-VS_2, the K_+/K_- valley is also sensitive to σ_+/σ_- circular polarized light. Like the in-plane electric field, the optical field can also produce the intrinsic SHE and OHE at two valleys, which means that the photo-generated electrons and holes by corresponding Hall effect carry the spin and orbital angular momentum [25,54]. Due to the SOC effect, the valley optical selection rule is spin-orbital polarized. By changing the polarization of incident light, we can select the valleys of excitation and thus selectively control the spin and orbital angular momentum directions in Table I.

V. TIME-REVERSAL SYMMETRY BREAKING

The VS_2 monolayer breaks the time-reversal and inversion symmetry at the same time. In this section, we will discuss the impact of time-reversal symmetry on spin-orbital polarization. Starting from the spin-orbital expectation valves $\langle \hat{L}_z \cdot \hat{S}_z \rangle_\tau^{s_z} = \tau s_z \hbar^2$ in $k \cdot p$ analysis, the valley-contrasting sign occurs when the spin polarizations at two valleys are the same. A significant SOC exists in a range of nonmagnetic orbital Hall insulators such as MoS_2 [25]. The bands at the time-reversal symmetry can be written as $E_n(\boldsymbol{k}) = E_n(-\boldsymbol{k})$, showing that the opposite spin will appear on two valleys at the case of time-reversal symmetry present, resulting in same sign of spin-orbital polarization at two valleys.

In Fig. 5, we choose VS_2 and MoS_2 as two special cases to investigate the impact of time-reversal symmetry breaking on the spin-orbital polarization. VS_2 exhibits opposite $\langle \hat{L}_z \cdot \hat{S}_z \rangle$,

TABLE I. Four states of the spin-orbital polarization in VS_2. The first and second arrows represent the directions of orbital and spin angular momentum, respectively.

	$s_z = +1$	$s_z = -1$
K_+ valley	↑↑	↑↓
K_- valley	↓↑	↓↓

as well as intrinsic SHE and OHE. The net magnetic moment breaks time-reversal symmetry, leading to spin splitting in the valence band. This induces electronic structures with the same spin polarization on the two valleys, resulting in the spin angular momentum of $\langle \hat{S}_z \rangle = \hbar/2$ for both valleys. Regarding MoS_2, although SOC effect induces spin splitting, the time-reversal symmetry present causes opposite $\langle \hat{S}_z \rangle$ in two valleys ($\langle \hat{S}_z \rangle = \pm\hbar/2$). Under the influence of SOC, the $\langle \hat{L}_z \cdot \hat{S}_z \rangle$ in Figs. 5(c) and 5(d) are the same in two valleys. The opposite spin-orbital polarizations appear in the highest valence band and the second highest valence band of MoS_2. According to Ref. [43], these two valence bands correspond to the peaks of A and B excitons. The simultaneous broken time-reversal and inversion symmetries is a crucial factor in generating opposite-sign spin-orbital polarization. Time-reversal symmetry breaking can induce an intrinsic spin magnetic moment and result in identical spin angular momentum in the valleys. The broken inversion symmetry creates valley orbital magnetic moments, leading to $\langle \hat{L}_z \rangle = \pm 2\hbar$ in two valleys. The SOC in TMDs couples the spin and orbital angular momentum into spin-orbital polarization, which generates $\langle \hat{L}_z \cdot \hat{S}_z \rangle$ under excitation by an electric field.

VI. CONCLUSION

Our $k \cdot p$ model and first-principles calculations show that the ferromagnetic TMDs exhibit opposite spin-orbital polarization at two valleys, which can be represented by intrinsic OHC and SHC. The broken inversion symmetry and SOC effect can host intrinsic valleys of spin-orbital polarization, with the sign of $\langle \hat{L}_z \cdot \hat{S}_z \rangle$ determining the spin and orbital angular momentum directions at both ends of the sample. Meanwhile, the time-reversal symmetry breaking causes the opposite-sign of $\langle \hat{L}_z \cdot \hat{S}_z \rangle$ on two valleys. Combined with spin-valley coupling, four spin-orbital polarization states exist in the system of ferromagnetic TMDs. Valley circular dichroism can replace the in-plane electric field to selectively excite carriers on the valleys of spin-orbital polarization under the conservation of

angular momentum. The combination of spin polarization and circularly polarized light can produce four directions of orbital and spin torques, thus accomplishing multi-state storage and operation of information. Our results illustrate the potential of ferromagnetic TMDs for applications in the direction of information storage and spin-orbitronics.

ACKNOWLEDGMENTS

This work is supported by National Natural Science Foundation of China (Grants No. 51872145 and No. 62174088), and Postgraduate Research and Practice Innovation Program of Jiangsu Province (Grants No. KYCX20_0748 and No. KYCX23_0977).

[1] O. Busch, I. Mertig, and B. Göbel, Orbital Hall effect and orbital edge states caused by s electrons, Phys. Rev. Res. **5**, 043052 (2023).

[2] Y. G. Choi, D. Jo, K. H. Ko, D. Go, K. H. Kim, H. G. Park, C. Kim, B. C. Min, G. M. Choi, and H. W. Lee, Observation of the orbital Hall effect in a light metal Ti, Nature (Lond.) **619**, 52 (2023).

[3] D. Go, D. Jo, C. Kim, and H. W. Lee, Intrinsic spin and orbital Hall effects from orbital texture, Phys. Rev. Lett. **121**, 086602 (2018).

[4] D. Go and H.-W. Lee, Orbital torque: Torque generation by orbital current injection, Phys. Rev. Res. **2**, 013177 (2020).

[5] H. Kontani, T. Tanaka, D. S. Hirashima, K. Yamada, and J. Inoue, Giant orbital Hall effect in transition metals: Origin of large spin and anomalous Hall effects, Phys. Rev. Lett. **102**, 016601 (2009).

[6] M. Zeer, D. Go, P. Schmitz, T. G. Saunderson, H. Wang, J. Ghabboun, S. Blügel, W. Wulfhekel, and Y. Mokrousov, Promoting p-based Hall effects by $p-d-f$ hybridization in Gd-based dichalcogenides, Phys. Rev. Res. **6**, 013095 (2024).

[7] I. Baek and H.-W. Lee, Negative intrinsic orbital Hall effect in group XIV materials, Phys. Rev. B **104**, 245204 (2021).

[8] S. Bhowal and S. Satpathy, Intrinsic orbital moment and prediction of a large orbital Hall effect in two-dimensional transition metal dichalcogenides, Phys. Rev. B **101**, 121112(R) (2020).

[9] L. M. Canonico, T. P. Cysne, A. Molina-Sanchez, R. B. Muniz, and T. G. Rappoport, Orbital Hall insulating phase in transition metal dichalcogenide monolayers, Phys. Rev. B **101**, 161409(R) (2020).

[10] Z. Chen, R. Li, Y. Bai, N. Mao, M. Zeer, D. Go, Y. Dai, B. Huang, Y. Mokrousov, and C. Niu, Topology-engineered orbital Hall effect in two-dimensional ferromagnets, Nano Lett. **24**, 4826 (2024).

[11] D. Jo, D. Go, and H.-W. Lee, Gigantic intrinsic orbital Hall effects in weakly spin-orbit coupled metals, Phys. Rev. B **98**, 214405 (2018).

[12] D. Go, D. Jo, H.-W. Lee, M. Kläui, and Y. Mokrousov, Orbitronics: Orbital currents in solids, Europhys. Lett. **135**, 37001 (2021).

[13] D. Lee, D. Go, H. J. Park, W. Jeong, H. W. Ko, D. Yun, D. Jo, S. Lee, G. Go, J. H. Oh, K. J. Kim, B. G. Park, B. C. Min, H. C. Koo, H. W. Lee, O. Lee, and K. J. Lee, Orbital torque in magnetic bilayers, Nat. Commun. **12**, 6710 (2021).

[14] A. Pezo, D. García Ovalle, and A. Manchon, Orbital Hall physics in two-dimensional dirac materials, Phys. Rev. B **108**, 075427 (2023).

[15] P. Wang, Z. Feng, Y. Yang, D. Zhang, Q. Liu, Z. Xu, Z. Jia, Y. Wu, G. Yu, X. Xu, and Y. Jiang, Inverse orbital Hall effect and orbitronic terahertz emission observed in the materials with weak spin-orbit coupling, npj Quantum Mater. **8**, 28 (2023).

[16] S. Ji, C. Quan, R. Yao, J. Yang, and X. Li, Reversal of orbital Hall conductivity and emergence of tunable topological quantum states in orbital Hall insulators, Phys. Rev. B **109**, 155407 (2024).

[17] S. Bhowal and G. Vignale, Orbital Hall effect as an alternative to valley Hall effect in gapped graphene, Phys. Rev. B **103**, 195309 (2021).

[18] T. P. Cysne, M. Costa, L. M. Canonico, M. B. Nardelli, R. B. Muniz, and T. G. Rappoport, Disentangling orbital and valley Hall effects in bilayers of transition metal dichalcogenides, Phys. Rev. Lett. **126**, 056601 (2021).

[19] T. P. Cysne, S. Bhowal, G. Vignale, and T. G. Rappoport, Orbital Hall effect in bilayer transition metal dichalcogenides: From the intra-atomic approximation to the Bloch states orbital magnetic moment approach, Phys. Rev. B **105**, 195421 (2022).

[20] K. Das and A. Agarwal, Intrinsic Hall conductivities induced by the orbital magnetic moment, Phys. Rev. B **103**, 125432 (2021).

[21] F. Xue, V. Amin, and P. M. Haney, Imaging the valley and orbital Hall effect in monolayer MoS_2, Phys. Rev. B **102**, 161103(R) (2020).

[22] M. Costa, B. Focassio, L. M. Canonico, T. P. Cysne, G. R. Schleder, R. B. Muniz, A. Fazzio, and T. G. Rappoport, Connecting higher-order topology with the orbital Hall effect in monolayers of transition metal dichalcogenides, Phys. Rev. Lett. **130**, 116204 (2023).

[23] G.-B. Liu, W.-Y. Shan, Y. Yao, W. Yao, and D. Xiao, Three-band tight-binding model for monolayers of group-VIB transition metal dichalcogenides, Phys. Rev. B **88**, 085433 (2013).

[24] W. Tong, S. Gong, X. Wan, and C. Duan, Concepts of ferrovalley material and anomalous valley Hall effect, Nat. Commun. **7**, 13612 (2016).

[25] D. Xiao, G. B. Liu, W. Feng, X. Xu, and W. Yao, Coupled spin and valley physics in monolayers of MoS_2 and other group-VI dichalcogenides, Phys. Rev. Lett. **108**, 196802 (2012).

[26] X. Zou, H. Ma, R. Li, Y. Dai, B. Huang, and C. Niu, Gate-mediated transition between antiferromagnetic topological and Chern insulators in honeycomb X_3MnN_3(X = Sr,Ba), Phys. Rev. B **106**, 075144 (2022).

[27] V. Vargiamidis, P. Vasilopoulos, and N. Neophytou, Tunable topological phases in monolayer Pt_2HgSe_3 with exchange fields, Phys. Rev. B **106**, 205416 (2022).

[28] M. Zeer, D. Go, J. P. Carbone, T. G. Saunderson, M. Redies, M. Kläui, J. Ghabboun, W. Wulfhekel, S. Blügel, and Y. Mokrousov, Spin and orbital transport in rare-earth dichalcogenides: The case of EuS_2, Phys. Rev. Mater. **6**, 074004 (2022).

[29] H. Chen, R. Liu, J. Lu, X. Zhao, G. Hu, J. Ren, and X. Yuan, Intrinsic valley-polarized quantum anomalous Hall effect and controllable topological phase transition in Janus Fe_2SSe, J. Phys. Chem. Lett. **13**, 10297 (2022).

[30] Q. Cui, Y. Zhu, J. Liang, P. Cui, and H. Yang, Spin-valley coupling in a two-dimensional VSi_2N_4 monolayer, Phys. Rev. B **103**, 085421 (2021).

[31] H. Huan, Y. Xue, B. Zhao, G. Gao, H. Bao, and Z. Yang, Strain-induced half-valley metals and topological phase transitions in MBr_2 monolayers (M = Ru, Os), Phys. Rev. B **104**, 165427 (2021).

[32] Z. F. Wang, Z. Liu, and F. Liu, Quantum anomalous Hall effect in 2D organic topological insulators, Phys. Rev. Lett. **110**, 196801 (2013).

[33] J. Zhou, Q. Sun, and P. Jena, Valley-polarized quantum anomalous Hall effect in ferrimagnetic honeycomb lattices, Phys. Rev. Lett. **119**, 046403 (2017).

[34] S. Kumar and S. Kumar, Ultrafast THz probing of nonlocal orbital current in transverse multilayer metallic heterostructures, Nat. Commun. **14**, 8185 (2023).

[35] H. Xie, N. Zhang, Y. Ma, X. Chen, L. Ke, and Y. Wu, Efficient noncollinear antiferromagnetic state switching induced by the orbital Hall effect in chromium, Nano Lett. **23**, 10274 (2023).

[36] D. Go, F. Freimuth, J.-P. Hanke, F. Xue, O. Gomonay, K.-J. Lee, S. Blügel, P. M. Haney, H.-W. Lee, and Y. Mokrousov, Theory of current-induced angular momentum transfer dynamics in spin-orbit coupled systems, Phys. Rev. Res. **2**, 033401 (2020).

[37] S. Ji, R. Yao, C. Quan, Y. Wang, J. Yang, and X. Li, Observing topological phase transition in ferromagnetic transition metal dichalcogenides, Phys. Rev. B **108**, 224422 (2023).

[38] R. Chen, D. Go, S. Blügel, W. Zhao, and Y. Mokrousov, Dzyaloshinskii-Moriya interaction from unquenched orbital angular momentum, Phys. Rev. B **109**, 144417 (2024).

[39] Y. Rouzhahong, C. Liang, C. Li, B. Wang, and H. Li, Valley piezoelectricity promoted by spin-orbit coupling in quantum materials, Sci. China Phys. Mech. Astron. **66**, 247711 (2023).

[40] D. J. Thouless, M. Kohmoto, M. P. Nightingale, and M. denNijs, Quantized Hall conductance in a two-dimensional periodic potential, Phys. Rev. Lett. **49**, 405 (1982).

[41] Y. Yao, L. Kleinman, A. H. MacDonald, J. Sinova, T. Jungwirth, D. S. Wang, E. Wang, and Q. Niu, First principles calculation of anomalous Hall conductivity in ferromagnetic bcc Fe, Phys. Rev. Lett. **92**, 037204 (2004).

[42] T. Adamantopoulos, M. Merte, D. Go, F. Freimuth, S. Blugel, and Y. Mokrousov, Orbital Rashba effect as a platform for robust orbital photocurrents, Phys. Rev. Lett. **132**, 076901 (2024).

[43] F. Caruso, M. Schebek, Y. Pan, C. Vona, and C. Draxl, Chirality of valley excitons in monolayer transition-metal dichalcogenides, J. Phys. Chem. Lett. **13**, 5894 (2022).

[44] X. Liu, A. P. Pyatakov, and W. Ren, Magnetoelectric coupling in multiferroic bilayer VS_2, Phys. Rev. Lett. **125**, 247601 (2020).

[45] X. Ma, L. Yin, J. Zou, W. Mi, and X. Wang, Strain-tailored valley polarization and magnetic anisotropy in two-dimensional 2H-VS_2/Cr_2C heterostructures, J. Phys. Chem. C **123**, 17440 (2019).

[46] C. Shen, G. Wang, T. Wang, C. Xia, and J. Li, Spin orientation and strain tuning valley polarization with magneto-optic Kerr effects in ferrovalley VS_2 monolayer, Appl. Phys. Lett. **117**, 042406 (2020).

[47] See Supplemental Material at http://link.aps.org/supplemental/10.1103/PhysRevB.110.075418 for DFT calculations, $k \cdot p$ model fitting results, ortbial contributions and spin-valley coupling of VS_2, and which includes Refs. [40,41,48,50,51,56–61],

[48] A. A. Mostofi, J. R. Yates, Y. S. Lee, I. Souza, D. Vanderbilt, and N. Marzari, wannier90: A tool for obtaining maximally-localised Wannier functions, Comput. Phys. Commun. **178**, 685 (2008).

[49] J. Qiao, J. Zhou, Z. Yuan, and W. Zhao, Calculation of intrinsic spin Hall conductivity by Wannier interpolation, Phys. Rev. B **98**, 214402 (2018).

[50] X. Wang, J. R. Yates, I. Souza, and D. Vanderbilt, *Ab initio* calculation of the anomalous Hall conductivity by Wannier interpolation, Phys. Rev. B **74**, 195118 (2006).

[51] Q. Wu, S. Zhang, H.-F. Song, M. Troyer, and A. A. Soluyanov, WannierTools: An open-source software package for novel topological materials, Comput. Phys. Commun. **224**, 405 (2018).

[52] Y. Wang, W. Wei, H. Wang, N. Mao, F. Li, B. Huang, and Y. Dai, Janus TiXY monolayers with tunable Berry curvature, J. Phys. Chem. Lett. **10**, 7426 (2019).

[53] A. Kormányos, V. Zólyomi, V. I. Fal'ko, and G. Burkard, Tunable Berry curvature and valley and spin Hall effect in bilayer MoS_2, Phys. Rev. B **98**, 035408 (2018).

[54] W. Yao, D. Xiao, and Q. Niu, Valley-dependent optoelectronics from inversion symmetry breaking, Phys. Rev. B **77**, 235406 (2008).

[55] P. Sahu, S. Bhowal, and S. Satpathy, Effect of the inversion symmetry breaking on the orbital Hall effect: A model study, Phys. Rev. B **103**, 085113 (2021).

[56] G. Kresse and D. Joubert, From ultrasoft pseudopotentials to the projector augmented-wave method, Phys. Rev. B **59**, 1758 (1999).

[57] G. Kresse and J. Furthmuller, Efficient iterative schemes for *ab initio* total-energy calculations using a plane-wave basis set, Phys. Rev. B **54**, 11169 (1996).

[58] P. E. Blochl, Projector augmented-wave method, Phys. Rev. B **50**, 17953 (1994).

[59] S. Grimme, J. Antony, S. Ehrlich, and H. Krieg, A consistent and accurate *ab initio* parametrization of density functional dispersion correction (DFT-D) for the 94 elements H-Pu, J. Chem. Phys. **132**, 154104 (2010).

[60] A. Rohrbach, J. Hafner, and G. Kresse, Electronic correlation effects in transition-metal sulfides, J. Phys.: Condens. Matter **15**, 979 (2003).

[61] T. Jungwirth, Q. Niu, and A. H. MacDonald, Anomalous Hall effect in ferromagnetic semiconductors, Phys. Rev. Lett. **88**, 207208 (2002).